Title
Effects of temperature on the shear strength of saturated sand

Journal
Soils and Foundations, 58(6)

ISSN
0385-1621

Authors
Liu, Hong
Liu, Hanlong
Xiao, Yang
et al.

Publication Date
2018-12-01

DOI
10.1016/j.sandf.2018.07.010

Peer reviewed

Elsevier Editorial System(tm) for Soils and Foundations
Manuscript Draft

Manuscript Number: SANDF-D-17-00421

Title: Effects of temperature on the shear strength of saturated sand

Article Type: Technical Paper

Keywords: temperature effects; undrained shear; critical state line; thermal expansion

Corresponding Author: Professor Yang xiao, Doctor

Corresponding Author's Institution: Chongqing University

First Author: Long H Liu, doctor

Order of Authors: Long H Liu, doctor; Hong Liu; Yang xiao, Doctor; John S McCartney, doctor

Abstract: The effect of temperature on the shear strength response of saturated, dense sand was investigated using a series of temperature-controlled, isotropically-consolidated, hollow cylinder triaxial compression tests, where specimens were heated in drained conditions followed by shearing in undrained conditions. The deviatoric stress at peak state (i.e., the undrained shear strength) was observed to increase with increasing initial mean effective stress as expected, but was observed to decrease linearly with increasing temperature. The temperature effects on the deviatoric stress at peak state were attributed to a linear decrease in the magnitude of negative shear-induced pore water pressure at peak conditions with temperature. The relations between the undrained shear strength and pore water pressure with the change in temperature were well-represented by linear equations. When the shear strength was interpreted in terms of critical state, no obvious changes in the critical state line in the plane were observed and the critical state friction angle was unaffected by temperature. During drained heating, the dense sand specimens were observed to expand volumetrically, causing the normal consolidation line in the plane to shift upwards with increasing temperature without a change in slope. The negative pore water pressures during undrained shearing caused the state paths for the dense sand specimens to move to the right. As the magnitude of negative pore water pressure decreased with increasing temperature, no obvious effects on the critical state line in the plane were observed.

Effects of temperature on the shear strength of saturated sand

Hanlong Liu [1], Hong Liu[2], Yang Xiao[3], John S. McCartney[4]

Abstract: The effect of temperature on the shear strength response of saturated, dense sand was investigated using a series of temperature-controlled, isotropically-consolidated, hollow cylinder triaxial compression tests, where specimens were heated in drained conditions followed by shearing in undrained conditions. The deviatoric stress at peak state (i.e., the undrained shear strength) was observed to increase with increasing initial mean effective stress as expected, but was observed to decrease linearly with increasing temperature. The temperature effects on the deviatoric stress at peak state were attributed to a linear decrease in the magnitude of negative shear-induced pore water pressure at peak conditions with temperature. The relations between the undrained shear strength and pore water pressure with the change in temperature were well-represented by linear equations. When the shear strength was interpreted in terms of critical state, no obvious changes in the critical state line in the $p'-q$ plane were observed and the critical state friction angle was unaffected by temperature. During drained heating, the dense sand specimens were observed to expand volumetrically, causing the normal consolidation line in the $e-\left(p'/p_{\mathrm{a}}\right)^{0.5}$ plane to shift upwards with increasing temperature without a change in slope. The negative pore water pressures during undrained shearing caused the state paths for the dense sand specimens to move to the right. As the magnitude of negative pore water pressure decreased with increasing temperature, no obvious effects on the critical state line in the $e-\left(p'/p_{\mathrm{a}}\right)^{0.5}$ plane were observed.

Keywords: temperature effects; undrained shear; critical state line; thermal expansion

----

1. Professor and Chair, School of Civil Engineering, Chongqing University, Chongqing, 400045, China. E-mail: cehliu@hhu.edu.cn

2. Ph.D. Candidate, School of Civil Engineering, Chongqing University, Chongqing, 400045, China. E-mail: cqulhong@163.com

3. Associate Professor, China Key Laboratory of New Technology for Construction of Cities in Mountain Area (Chongqing University), Ministry of Education, Chongqing, 400045, China; Associate Professor, School of Civil Engineering, Chongqing University, Chongqing, 400045, China. E-mail: hhuxyanson@163.com (Corresponding author)

4. Associate Professor, Department of Structural Engineering, University of California San Diego, 9500 Gilman Drive, La Jolla, CA, 92093-0085, USA. Email: mccartney@ucsd.edu

Introduction

A clear understanding of the thermo-mechanical behavior of soils is critical due to the range applications in geotechnical engineering where significant temperature changes may be encountered. Examples of such applications include nuclear waste repositories (Gens et al. 2009), high voltage electric cables (Brandon et al. 1989), energy piles (Knellwolf et al. 2011; Liu et al. 2016a; Olgun and McCartney 2014), thermally-active embankments (Coccia and McCartney 2013), thermally-active retaining walls (Stewart et al. 2014), highway pavements (Kertesz and Sansalone 2014), and geothermal tunnel linings (Brandl 2006). In these applications, an understanding of the shear strength of soils is needed, both in terms of the undrained shear strength in the case that a total stress analysis is performed and in terms of the drained shear strength parameters or critical state parameters in the case that an effective stress analysis is performed. The impact of temperature on the shear strength of soils in either of these analyses depends on whether heating occurs in undrained or drained conditions, and whether shearing is performed in undrained or drained conditions. During undrained heating or shearing, pore water pressures in the soil may change, leading to changes in effective stress, while during drained heating or shearing, volume changes may occur.

In the case of undrained heating, the pore water pressure of all soils is expected to increase as a result of differences in the coefficients of thermal expansion of the pore water and solid skeleton (Campanella and Mitchell 1968; Bruyn and Thimus 1996; Houston et al. 1985; Uchaipichat and Khalili 2009), leading to a decrease in the effective stress and elastic expansion. However, during drained heating of the soil, volume change of soils will occur with a magnitude and sign dependent on the initial state. For example, in previous studies focused on heating saturated clay or silt under drained conditions (Abuel-Naga et al. 2006; Cekerevac and Laloui 2004; Graham et al. 2001), changes in volume were observed to occur that depend on the stress history quantified using the overconsolidation ratio (OCR).

Specifically, a transition from contractive to expansive behavior during drained heating is typically observed as the OCR of clays or silts increases. Fewer studies have been performed on the thermal volume change of sands. Ng et al. (2016) observed that when heating sands in drained conditions, changes in volume may occur that depend on the relative density. Similar to the effects of the OCR, sands have been observed to show a similar transition from contractive to expansive behavior during drained heating with increases in relative density (Ng et al. 2016).

After undergoing undrained or drained heating, soil specimens may be sheared under drained conditions (e.g., Hueckel and Baldi 1990; Cekerevac and Laloui 2004; Uchaipichat and Khalili 2009) or undrained conditions (e.g., Houston et al. 1985; Kuntiwattanakul et al. 1995; Abuel-Naga et al. 2006, 2009). Regardless of the drainage conditions during shear, most studies conclude that the temperature does not have a major effect on the the drained friction angle (Laloui 2001), the compression indices (Campanella and Mitchell 1968), or the critical state line (Cekerevac and Laloui 2004). Nevertheless, the undrained shear strength may be affected by several other variables, including temperature effects on the shear-induced pore water pressure (Abuel-Naga et al. 2006; Bruyn and Thimus 1996; Cekerevac and Laloui 2004; Houston et al. 1985). Houston et al. (1985) evaluated the undrained shear strength of seafloor sediments using isotropic triaxial tests at different temperatures. They observed that an increase in mean effective stress leads to an increase in peak shear strength, as expected, while drained heating under increasing temperatures led to increases in peak shear strength. Kuntiwattanakul et al. (1995) observed that the undrained shear strength of the normally-consolidated Kaolinite clay depended on the drainage conditions during heating. Due to the positive pore water pressure during undrained heating, the undrained shear strength of soils tested after undrained heating was consistently lower than the undrained shear strength of soils after drained heating. Similar investigations of the impact of drainage conditions on the shear strength of sands after heating have not been performed.

The main objective of this paper is to evaluate the effects of temperature on the shear strength behavior of saturated, dense sand specimens using a series of temperature-controlled hollow triaxial tests under different values of mean effective stress and temperature. Variables measured include the shear stress-strain and pore water pressure relationships, which can be used to infer the deviatoric stress at peak state, initial secant modulus, normal consolidation line, critical state friction angle, and critical state line. Although dense sands are expected to show volumetric expansion during shearing without much plastic strain, the effects of temperature on the shear-induced pore water pressure in sands are not well understood and may play an important role in their thermo-mechanical response.

Testing program

The schematic diagrams of the temperature sensor arrangement and the overall hollow cylinder triaxial apparatus with temperature controlled are shown in Fig. 1(a) and Fig. 1(b). Three temperature sensors (i.e., T1, T2 and T3) are set as shown in Fig. 1(a) to measure the bottom, top and inner temperatures of the hollow cylinder sand specimens, respectively. The average value of the top and bottom temperatures measured by T2 and T1 is defined as the outer temperature of specimens, and the inner temperature of specimens is calculated by temperature sensor T3 directly. To reach a uniform temperature in soils, the differences between the outer, inner and target temperatures should be smaller than 0.5 °C. The details of the apparatus were described in Liu et al. (2016b).

The sand used in the temperature-controlled hollow cylinder triaxial tests is from Fujian, China, with a representative sample shown in Fig. 1(c). The main component of this material is SiO_2, approximately 96% by mass. As shown in Fig. 1(d), the mean grain size D_{50} is 0.60 mm, the coefficient of uniformity C_u is 7.05 and the coefficient of curvature C_c is 0.54.

The minimum and maximum void ratios are 0.335 (ASTM 2014a) and 0.708 (ASTM 2014b), respectively.

The hollow cylinder specimens have an outer diameter of 100 mm, an inner diameter of 60 mm, and a height of 200 mm. All the sand specimens were prepared by the water sedimentation method to reach a dense state with a relative density D_r of 90%. This corresponds to an initial void ratio of 0.373, which was the same for all the specimens evaluated in this study. Three mean effective stress values of p'_0=50 kPa, 100 kPa and 200 kPa were used in the hollow cylinder triaxial tests. For each mean effective stress, four different temperatures (T=25 °C, 35 °C, 45 °C and 55 °C) were applied in drained conditions to investigate the influence of temperature on the undrained shear strength behavior of saturated sand. A heating rate of 3.33 °C/h, was selected to ensure drained conditions. This was the same rate used by Cekerevac and Laloui (2004), who tested a kaolinite clay with much lower hydraulic conductivity than the dense sand tested in this study.

The stress paths of the temperature-controlled triaxial tests are shown in Fig. 1(e). These paths include four stages, including saturation, drained mechanical consolidation (i.e., 0-1), drained heating (also referred to as thermal consolidation) (i.e., 1-2) and undrained shearing (i.e., 1-4 and 2-3) stages.

Test Results

Thermal volume change

The relationship between the thermal volumetric strain of the sand at an initial relative density of 90% (corrected to account for the thermal expansion of the drainage system) and the change in temperature is shown in Figure 2. Although there is some variability in the thermal volume change at the highest temperature investigated, the results are well described by the following linear relationship:

$$\varepsilon_{\mathrm{vt}} = k_{\mathrm{vt}}\left(T - T_0\right) \tag{1}$$

where $\varepsilon_{\mathrm{vt}}$ is the thermal volumetric strain and k_{vt} is the volumetric coefficient of thermal expansion defined such that positive thermal volumetric strain values denote compression. The value of k_{vt} in Equation (1) was found to be -0.00007/°C, and is listed in Table 2 with the other model parameters. The dense sand specimens showed expansion during drained heating, leading to an increase in void ratio, and the mean effective stress did not have a major effect on the thermal volume change. It should be noted that the value of k_{vt} for the dense sand is about 3.5 times smaller than that of water (-0.000241/°C), indicating that drained heating of the dense sand is likely controlled by the soil skeleton. A more detailed description of the thermal volume change measurements can be found in Liu et al. (2016b).

Shear stress-strain relationships

The shear stress-strain relationships of the sand specimens after mechanical consolidation to different mean effective stresses and drained heating to different temperatures are shown in Figures 3 and 4. The shear stress is presented in terms of the deviatoric stress (i.e., $q = \sigma_1' - \sigma_3'$). Evaluation of the results in Figure 3 indicates that the deviatoric stress at peak conditions decreases with increasing temperature for a given mean effective stress, while evaluation of the results in Figure 4 indicates that the deviatoric stress at peak conditions increases with increasing mean effective stress for a given temperature.

The shear-induced pore water pressure was consistently observed to be positive at the beginning of undrained shearing, reflecting the tendency for the soil to initially contract volumetrically. However, after an axial strain of approximately 0.5% the shear-induced pore water pressures were negative, reflecting the tendency for the soil to dilate volumetrically. The tendency for dilation resulting in negative pore water pressures during undrained shear is expected for this sand with a relatively high relative density of 90%. The results in Figure 3 indicate that for each set of specimens at a given initial mean effective stress, lower shear-induced excess pore water pressures at peak conditions were observed with increasing temperatures. On the other hand, the results in Figure 4 indicate that for each set of specimens at a given change in temperature, lower shear-induced pore water pressures at peak conditions were observed for specimens with lower initial mean effective stresses. In general, the pore water pressure is almost constant at end of the experiments (axial strain of approximately 20%), which indicates that most of the specimens have reached critical state (i.e., steady state conditions). However, the deviatoric stress values are observed to continue decreasing with increasing axial strain. The trends in deviatoric stress at high axial strains may be not a real material behavior, but may be a result of nonhomogeneous deformation which is usually seen in triaxial tests for dense sand due to end restraint effects (Chu and Sik-Cheung 1993).

Deviatoric stress at peak state

The relationships between the deviatoric stress at peak state (i.e., the undrained shear strength) and the change in temperature are shown in Fig. 5. The trends in the data can be represented using the following linear relationship:

$$q_{\mathrm{ps}} = q_{\mathrm{ps0}} + a\left(T - T_0\right) \qquad (2)$$

where q_{ps} and q_{ps0} are the deviatoric stresses at peak state, as the sand specimens are heated to the target and initial ambient room temperatures, respectively; T is the target temperature; T_0 is the initial room temperature (i.e., T_0=25 $^{\mathrm{o}}$C) and a is a material constant. The values of q_{ps0} and a are listed in Table 2. It can be observed that the deviatoric stress at peak state (i.e., the undrained shear strength) increases with mean effective stress, while an increase in temperature leads to a reduction in deviatoric stress at peak state. These results indicate that the deviatoric stress at peak state is lower after drained heating than at the initial room temperature. Therefore, drained heating of saturated, dense sands is expected to lead to a decrease in the undrained shear strength.

Shear-induced pore water pressures at peak state

The shear-induced pore water pressure at peak state was observed to decrease with increasing temperature, as shown in Figure 6. This trend in the data can be described using the following linear relationship:

$$u_{\mathrm{ps}} = u_{\mathrm{ps0}} + b\left(T - T_0\right) \tag{3}$$

where u_{ps} and u_{ps0} are the peak state pore water pressures at target and initial ambient room temperatures, respectively; b is material constant. The values of u_{ps0} and b are listed in Table 2.

The source of the observed temperature effects on the shear-induced pore water pressure at peak state may be due to changes in compressibility of the pore water and the soil skeleton with temperature. It is well-known that for small strain (elastic) conditions, the change in pore water pressure during undrained shearing is related to the compression coefficient of pore water and soil skeleton in saturated sand specimens, as follows:

$$\Delta u = \frac{\Delta q}{3\left[1 + n\left(m_{\mathrm{w}}/m_{\mathrm{s}}\right)\right]} \tag{4}$$

where Δu is the shear-induced change in pore water pressure; Δq is the change in deviatoric stress; n is porosity; m_{w} and m_{s} are the coefficients of volume compressibility of the pore water and soil skeleton, respectively. If the values of m_{w} and m_{s} vary with temperature, then this equation may help explain the lower changes in pore water pressure.

Dorsey and Ernest (1940) observed that as temperature increased from 0 to 38 $^{\circ}$C, the bulk modulus of water at atmospheric pressure increased from 195 to 229 MPa. Even though the maximum temperature applied in this study of 55 $^{\circ}$C is slightly over the temperature range used in Dorsey and Ernest (1940), it may be reasonable to conclude that the bulk modulus of water will increase with increasing temperature (and that coefficient of volume compressibility of pore water used in Eq. (4) would decrease). This may be the mechanism behind the temperature effects on the shear-induced changes in pore water pressure observed in this study.

Initial secant modulus

The initial secant modulus at an axial strain of 0.5% was calculated from the stress-strain curves for different mean effective stress and temperature conditions, which was a similar approach used by Cekerevac and Laloui (2004). The results in Figure 7 indicate that the increasing mean effective stress contributes to an increase in initial secant modulus. Although there are some slight variations, the initial secant modulus is relatively constant with temperature for dense sand specimens.

Critical state friction angle

The critical state friction angle is defined as follows:

$$\sin\varphi_{\mathrm{cs}} = \frac{\sigma'_{1\mathrm{cs}} - \sigma'_{3\mathrm{cs}}}{\sigma'_{1\mathrm{cs}} + \sigma'_{3\mathrm{cs}}} \tag{5}$$

where φ_{cs} is the friction angle at critical state, and $\sigma'_{1\mathrm{cs}}$ and $\sigma'_{3\mathrm{cs}}$ are the major and minor effective principal stresses at critical state, respectively. Unfortunately, a well-defined critical state condition is not always reached due to the nonhomogeneous deformation and other testing effects (Charles and Watts 1980; Chu and Sik-Cheung 1993), and it is sometimes necessary to extrapolate the experimental data to a most probable critical state (Charles and Watts 1980). However, it may be difficult for dense or very loose sand specimens to reach critical state, even though the test has been performed to a relatively high axial strain. In this case, Chu and Sik-Cheung (1993) conducted a series of post-failure undrained tests for dense granular soils to measure the critical state parameters. They found out that a constant effective stress ratio (i.e., q/p') for different mean effective stresses can be observed by end of most triaxial compression tests, and at the same time, the pore water pressure also approaches a constant value. Carrera et al. (2011) estimated a 'most probable' value of stress ratio at the critical state (i.e., $(q/p')_{\mathrm{cs}}$) from the stress-dilatancy curve for the drained and undrained tests. For undrained shearing tests, the rate of change in pore water pressure (i.e., $\Delta u/\Delta\varepsilon_{\mathrm{a}}$) was used to evaluate dilatancy. In this study, the critical state condition is determined by the methods of Carrera et al. (2011). The relationship of the stress ratio and dilatancy for an undrained test (i.e., p'=50 kPa, T=25 $^{\mathrm{o}}$C) is shown in Figure 8. The stress ratio (q/p') increases with an increase in axial strain, and then decreases gradually during the undrained shearing phase. The point of the intersection of the zero dilatancy axis and the last part of the curve is predicted as the stress ratio at the critical state (i.e., $(q/p')_{\mathrm{cs}}$). Further, the mean effective stress p'_{cs} can be obtained from the $q-p'$ graph as shown in Figure 9, once the $(q/p')_{\mathrm{cs}}$ is known. Therefore, the critical state condition for the dense sands evaluated in this study is assumed to correspond the condition in which the last part of the curve intersects the zero dilatancy axis. The critical state points for all the tests were obtained using this method, and are also shown in Figures 3 and 4. The corresponding values of critical state friction angle corresponding to these points are listed in Table 1. It is observed that the friction angles at critical state for the saturated, dense sand specimens are independent of the temperature and mean effective stress.

Discussion

The normal consolidation lines (NCLs) plotted in the $e-(p'/p_{\mathrm{a}})^{0.5}$ plane at different temperatures are shown in Figure 10. The data shows that there is a clear upward shift in the

NCLs with temperature due to the linear thermal expansion described by Equation (1). The NCL data can be described by a linear relationship, as follows:

$$e_{\mathrm{c}} = N - \lambda_{\mathrm{c}} \left(p' / p_{\mathrm{a}} \right)^{0.5} \tag{6}$$

where e_{c} is the void ratio of a saturated, dense sand specimen after thermal consolidation; p_{a} is the atmospheric pressure of 101 kPa, N is the intercept of the normal consolidation line and may depend on temperature based on Equation (1); and λ_{c} is the gradient of the normal consolidation line which is assumed to be constant with temperature. The values of N and λ_{c} are listed in Table 2.

The thermal volumetric strain is also defined as follows:

$$\varepsilon_{\mathrm{vt}} = -\frac{\Delta e}{1 + e_{\mathrm{c0}}} \times 100\% \tag{7}$$

where Δe is the difference between the void ratio of the dense sand specimens after thermal consolidation; e_{c0} is the void ratio of specimens before thermal consolidation. The combination of Equations (1) and (7) gives:

$$\Delta e = -k_{\mathrm{vt}} \left(1 + e_{\mathrm{c0}} \right) \left(T - T_0 \right) \tag{8}$$

Due to the negative volumetric coefficient of thermal expansion (i.e., k_{vt}=-0.00007/$^{\circ}$C) mentioned above, it can be observed that the change in void ratio of the dense sand specimens calculated form Equation (8) is positive. The void ratio of the specimens increases with increasing temperature, and the respective NCLs shift upward with temperature. Moreover, the NCLs of saturated, dense sand specimens (as shown in Figure 10) are spaced equally based on the form of Equation (8).

Further, the critical state line in the $p' - q$ plane for different mean effective stresses and temperatures is shown in Figure 11, and can be fitted by a linear equation, as follows:

$$q = M_{\mathrm{cs}} p' \tag{9}$$

where M_{cs} is material constant. The value of the constant for Fujian sand at an initial D_r of 90% is listed in Table 2. The average critical state friction angle $\bar{\varphi}_{cs}$ for dense sand can be calculated from M_{cs} as follows:

$$\sin \bar{\varphi}_{cs} = \frac{3M_{cs}}{6+M_{cs}} \tag{10}$$

The critical state friction angle $\bar{\varphi}_{cs}$ calculated from the best-fit value of M_{cs} in Fig. 11 using Equation (10) is 37.1^o for the dense sand specimens. This value is very close to the average value of the critical state friction angles calculated from the individual experiments using Equation (5). Similar to the observation from the values of φ_{cs} in Table 1, the good fit of Equation (9) to the experimental data observed in Figure 11 confirms that $\bar{\varphi}_{cs}$ does not change with temperature.

The critical state line (CSL) for the dense sand specimens in the $e-\left(p'/p_a\right)^{0.5}$ plane (Li and Wang 1998) at different temperatures are shown in Figure 12. The CSL can be expressed as follows:

$$e_{cs} = \Gamma - \lambda_{cs}\left(p'/p_a\right)^{0.5} \tag{11}$$

where e_{cs} is the void ratio of a sand specimen at critical state; Γ is the intercept of the critical state line; and λ_{cs} is the gradient of the CSL. The values of Γ and λ_{cs} are listed in Table 2. Different form the value of e_c in the NCLs, the value of e_{cs} does not increase significantly with temperature. This is possibly because the magnitude of negative pore water pressure generation decreases in tests at higher temperatures. Some variability in the trend in e_{cs} with temperature is observed because of the assumption regarding the point of critical state in the dense sand specimens.

The value of e_{cs} in the volumetric plane are bounded by two limit lines, as shown in

Figure 12. The upper boundary of the critical state points is defined as the UF line, and the lower one is the LF line (Konrad 1990). The slopes of the UF and LF lines are equal to that of the CSL with a value of 0.008. The intercepts of the NCLs (i.e. N) in the volumetric plane shift upward with increasing temperature, because of thermal expansion of the dense sand specimens. However, the CSL is approximately the same for all the specimens at different initial mean effective stresses and temperatures. No obvious changes in the intercept and slope of the CSL for saturated, dense sand specimens are observed with temperature.

Conclusions

A series of temperature-controlled hollow triaxial tests were carried out to investigate the thermally-induced strength behavior of saturated, dense sand. The deviatoric stress at peak state was observed to decrease linearly with changes in temperature. The temperature had no major impact on the initial secant modulus for dense sand. In addition, the critical state line in the $p'-q$ plane was not dependent on temperature, which was consistent with previous studies. Consistent with previous observations from tests on clay soils, the slopes of the NCL and CSL were observed to be equal and not affected by temperature. Due to the upward shift in the NCL caused by the thermal expansion of the sand specimens during drained heating, the intercept of the NCL in $e-\left(p'/p_{\mathrm{a}}\right)^{0.5}$ plane was observed to increase with temperature. However, due to the linear decrease in the shear-induced pore water pressure with temperature, the intercept of the CSL was observed to not depend significantly on temperature.

Acknowledgments

The authors would like to acknowledge the financial support from the Project supported by the National Natural Science Foundation of China (Grant No. 51678094 and Grant No. 51509024), and the Project funded by China Postdoctoral Science Foundation (Grant No.

2016M590864). The last author would like to acknowledge financial support from the US National Science Foundation project CMMI 1054190.

Notation

The following symbols are used in this paper:

D_{50} =Mean grain size (mm);

C_{u} =Coefficient of uniformity;

C_{c} =Coefficient of curvature;

D_{r} =Relative density (%);

$\varepsilon_{\mathrm{vt}}$ =Thermal volumetric strain (%);

e =Void ratio;

Δe =Change in void ratio;

e_{c} =Void ratio after thermal consolidation conditions;

e_{c0} =Void ratio before thermal consolidation conditions;

e_{cs} =Void ratio at critical state;

p' = Mean effective stress (kPa);

p'_0 = Initial mean effective stress (kPa);

p_{a} =Atmospheric stress (kPa);

q = Deviatoric stress (kPa);

q/p' =Effective stress ratio;

q_{ps} = Peak state deviatoric stress at target temperature (kPa);

q_{ps0} = Peak state deviatoric stress at initial room temperature (kPa);

u_{ps} = Peak state pore water pressure at target temperature (kPa);

u_{ps0} = Peak state pore water pressure at initial room temperature (kPa);

Δu = Pore water pressure (kPa);

Δq = Change in deviatoric stress (kPa);

n = Porosity;

m_w = Volume compression coefficient of pore water (/kPa);

m_s = Volume compression coefficient of soil skeleton (/kPa);

σ_1' = Major effective principal stress (kPa);

σ_3' = Minor effective principal stress (kPa);

σ_{1cs}' = Major effective principal stress at critical state (kPa);

σ_{3cs}' = Minor effective principal stress at critical state (kPa);

T = Target temperature (°C);

T_0 = Initial ambient room temperature (°C);

E = Initial secant modulus (MPa);

φ_{cs} =Friction angle at critical state (^{o});

$\bar{\varphi}_{cs}$ =Average friction angle at critical state (^{o});

a, b, k_{vt}, M_{cs}, N, Γ, λ_c and λ_{cs} =Constants.

References

Abuel-Naga, H. M., Bergado, D. T., Ramana, G. V., Grino, L., Rujivipat, P., and Thet, Y. (2006): Experimental evaluation of engineering behavior of soft Bangkok clay under elevated temperature. *Journal of Geotechnical and Geoenvironmental Engineering*, **132**(7): 902-910.

Abuel-Naga, H. M., Bergado, D. T., Bouazza, A., and Pender, M. (2009): Thermomechanical model for saturated clays. *Géotechnique*, **59**(3): 273-278.

ASTM D4253, 2014a. Standard: Standard test methods for maximum index density and unit weight of soils using a vibratory table. *Annual Book of ASTM Standards*, ASTM International, West Conshohocken, PA, 1-14.

ASTM D4254, 2014b. Standard: Standard test methods for minimum index density and unit weight of soils and calculation of relative density. *Annual Book of ASTM Standards*, ASTM International, West Conshohocken, PA, 1-9.

Brandl, H. (2006): Energy foundations and other thermo-avtive ground structures. *Geotechnique*, **56**(2): 81-122.

Brandon, T. L., Mitchell, J. K., and Cameron, J. T. (1989): Thermal instability in buried cable backfills. *Journal of Environmental Engineering*, **115**(1): 38-55.

Bruyn, D. D., and Thimus, J. F. (1996): The influence of temperature on mechanical characteristics of Boom clay-the results of an initial laboratory program. *Engineering Geology*, **41**: 117-126.

Campanella, R. G., and Mitchell, J. K. (1968): Influence of temperature variations on soil behaviour. *Journal of the Soil Mechanics and Foundation Division*, **94**(3): 709-734.

Carrera, A., Coop, M., and Lancellotta, R. (2011): Influence of grading on the mechanical behaviour of Stava tailings. *Geotechnique*, **61** (11): 935-946.

Cekerevac, C., and Laloui, L. (2004): Experimental study of thermal effects on the mechanical behaviour of a clay. *International Journal for Numerical and Analytical Methods in Geomechanics*, **28**(3): 209-228.

Charles, J. A., and Watts, K. S. (1980): The influence of confining pressure on the shear strength of compacted rockfill. *Geotechnique*, **30**(4): 353-367.

Chu, J., and Sik-Cheung, R. L. (1993): On the measurement of critical state parameters of dense granular soils. *Geotechnical Testing Journal*, **16**(1): 27-35.

Coccia, C. J. R. and McCartney, J. S. (2013): Impact of heat exchange on the thermo-hydro-mechanical response of reinforced embankments. *Proceedings of GeoCongress 2013*, ASCE. San Diego, CA. Mar. 3-5: 343-352.

Dorsey, Ernest, N. (1940): Properties of ordinary water-substance. *Reinhold Publishing Corp.*, New York, N. Y., Table 105, 243.

Gens, A., Sánchez, M., Guimarães, L. D. N., Alonso, E. E., Lloret, A., Olivella, S., Villar, M. V., and Huertas, F. (2009): A full-scale in situ heating test for high-level nuclear waste disposal: observations, analysis and interpretation. *Géotechnique*, **59**(4): 377-399.

Graham, J., Tanaka, N., Crilly, T., and Alfaro, M. (2001): Modified Cam-Clay modelling of temperature effects in clays. *Canadian Geotechnical Journal*, **38**(3): 608-621.

Houston, S. L., Houston, W. N., and Williams, N. D. (1985): Thermo-mechanical behavior of seafloor sediments. *Journal of Geotechnical Engineering*, **111**(11): 1249-1263.

Hueckel, T., Baldi, G. (1990): Thermoplasticity of saturated clays: experimental constitutive study. *Journal of Geotechnical Engineering*, **116**(12): 1778-1796.

Kertesz, R., and Sansalone, J. (2014): Hydrologic transport of thermal energy from pavement. *Journal of Environmental Engineering*, **140**(8): 04014028.

Knellwolf, C., Peron, H., and Laloui, L. (2011): Geotechnical analysis of heat exchanger piles. *Journal of Geotechnical and Geoenvironmental Engineering*, **137**(10): 890-902.

Konrad, J. M. (1990): Minimum undrained strength versus steady-state strength of sands.

Journal of Geotechnical Engineering, **116**(6): 948-963.

Kuntiwattanakul, P., Towhata, I., Ohishi, K. and Seko, I. (1995): Temperature effects on undrained shear characteristics of clay. *Soils and Foundations*, **35**(1): 147-162.

Laloui, L. (2001): Thermo-mechanical behaviour of soils. RFGC (*French Revue of Civil Engineering*), **5**(6): 809-843.

Li, X. S., and Wang, Y. (1998): Linear representation of steady-state line for sand. *Journal of Geotechnical and Geoenvironmental Engineering*, **124**(12): 1215-1217.

Liu, H., Liu, H. L., Xiao, Y., and McCartney, J. S. (2016b): Influence of temperature on the volume change behavior of saturated sand. *Geotechnical Testing Journal*, Accepted.

Liu, H. L., Wang, C. L., Kong, G. Q., Charles, W. W. Ng, and Che P. (2016a): Model tests on thermo-mechanical behavior of an improved energy pile. *European Journal of Environmental and Civil Engineering*, 1-16.

Ng, C. W. W., Wang, S. H., and Zhou, C. (2016): Volume change behaviour of saturated sand under thermal cycles. *Géotechnique Letters*, **6**(2): 124-131.

Olgun, C. G., and McCartney, J. S. (2014): Outcomes from international workshop on thermoactive geotechnical systems for near-surface geothermal energy: from research to practice. *The Journal of the Deep Foundations Institute*, **8**(2): 59-73.

Stewart, M.A., Coccia, C.J.R., and McCartney, J.S. (2014): Issues in the implementation of sustainable heat exchange technologies in reinforced, unsaturated soil structures. *Proc. GeoCongress 2014 (GSP 234)*, M. Abu-Farsakh and L. Hoyos, eds. ASCE: 4066-4075.

Uchaipichat, A., and Khalili, N. (2009): Experimental investigation of thermo-hydro-mechanical behaviour of an unsaturated silt. *Géotechnique*, **59**(4): 339-353.

Table Caption List:

Table 1

Table. 1. Details of the experimental program

Number	Mean effective stress p' : kPa	Applied temperature T: °C	Initial void ratio e_0	Thermal volumetric strain ε_v : %	Critical state friction angle φ_{cs} : °
1	50	25	0.372	0.000	37.5
2		35	0.370	-0.073	37.8
3		45	0.375	-0.141	37.2
4		55	0.371	-0.221	37.4
5	100	25	0.376	0.000	37.5
6		35	0.375	-0.074	37.6
7		45	0.373	-0.132	37.2
8		55	0.370	-0.170	37.8
9	200	25	0.375	0.000	36.9
10		35	0.372	-0.072	36.2
11		45	0.370	-0.145	36.3
12		55	0.374	-0.242	37.1

Table 2

Table. 2. Values of constants

Equation number	Symbol	Unit	Value
(1)	k_{vt}	/ ºC	-0.00007
(2)	q_{ps0}^{50}	kPa	1270.60
	q_{ps0}^{100}		1506.84
	q_{ps0}^{200}		1625.65
	a	kPa/ºC	-4.68
(3)	u_{ps0}^{50}	kPa	-363.45
	u_{ps0}^{100}		-377.85
	u_{ps0}^{200}		-354.93
	b	kPa/ºC	1.45
(6)	N_{25}	-	0.376
	N_{35}		0.377
	N_{45}		0.378
	N_{55}		0.379
	λ_{c}		0.008
(9)	M_{cs}	-	1.510
(11)	Γ	-	0.377
	λ_{cs}		0.008

Figure Caption List:

Fig. 1 Testing programs of the temperature-controlled hollow cylinder triaxial compression tests: (a) Schematic diagram of the temperature sensor arrangement; (b) Schematic diagram of the temperature-controlled hollow triaxial apparatus; (c) Photo of Fujian sand; (d) Particle size distribution; (e) Testing paths evaluated for Fujian sand

Fig. 2. Relationship between the thermal volumetric strain and change in temperature

Fig. 3 Stress-strain relationships for sand in temperature-controlled hollow cylinder triaxial tests under different temperature conditions: (a) p_0'=50 kPa; (b) p_0'=100 kPa; (c) p_0'=200 kPa

Fig. 4 Stress-strain relationships for sand in temperature-controlled hollow cylinder triaxial tests under different mean effective stress conditions: (a) T=25 ºC; (b) T=35 ºC; (c) T=45 ºC; (d) T=55 ºC

Fig. 5 Impact of the change in temperature on the deviatoric stress at peak state along with best-fit trendlines

Fig. 6 Impact of the change in temperature on the pore water pressure at peak state along with best-fit trendlines

Fig. 7 Impact of temperature on the initial secant modulus

Fig. 8 Estimation of the stress ratio at critical state by means of the rate of pore water pressure change graph

Fig. 9 Estimation of p_{cs}' in the $p'-q$ plane

Fig. 10 Normal consolidation lines for dense sand specimens in the $e-(p'/p_a)^{0.5}$ plane

Fig. 11 Critical state line for dense sand specimens in the $p'-q$ plane (not to scale)

Fig. 12 Critical state line for dense sand specimens in the $e-\left(p'/p_{\mathrm{a}}\right)^{0.5}$ plane

Figure 1

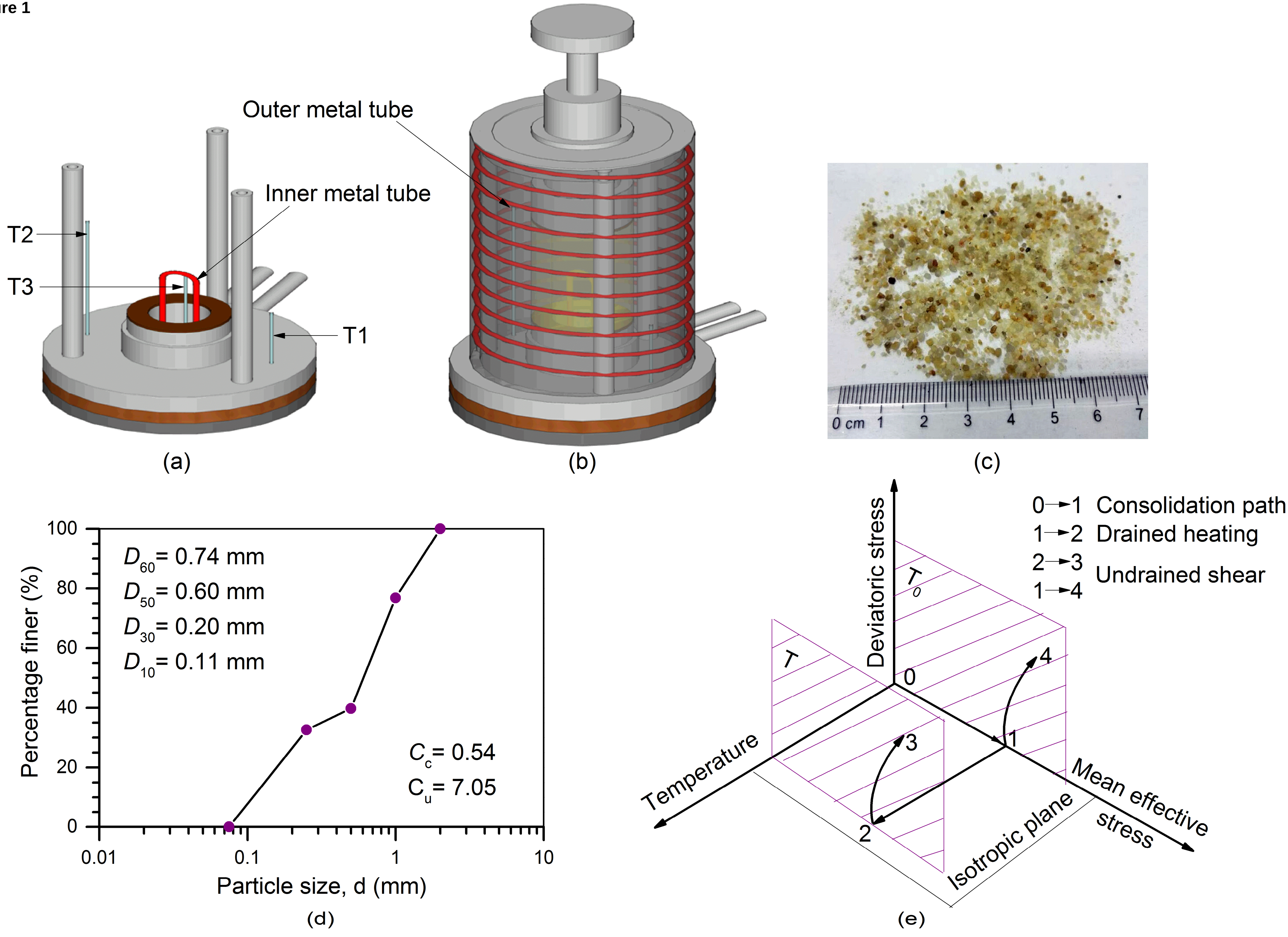

Outer metal tube
Inner metal tube
T2
T3
T1
(a)
(b)
0 cm 1 2 3 4 5 6 7
(c)
D_{60}= 0.74 mm
D_{50}= 0.60 mm
D_{30}= 0.20 mm
D_{10}= 0.11 mm
C_c= 0.54
C_u= 7.05
Percentage finer (%)
100
80
60
40
20
0
0.01
0.1
1
10
Particle size, d (mm)
(d)
Deviatoric stress
0→1 Consolidation path
1→2 Drained heating
2→3
1→4 Undrained shear
T_0
T
0
1
2
3
4
Temperature
Mean effective stress
Isotropic plane
(e)

Figure 2

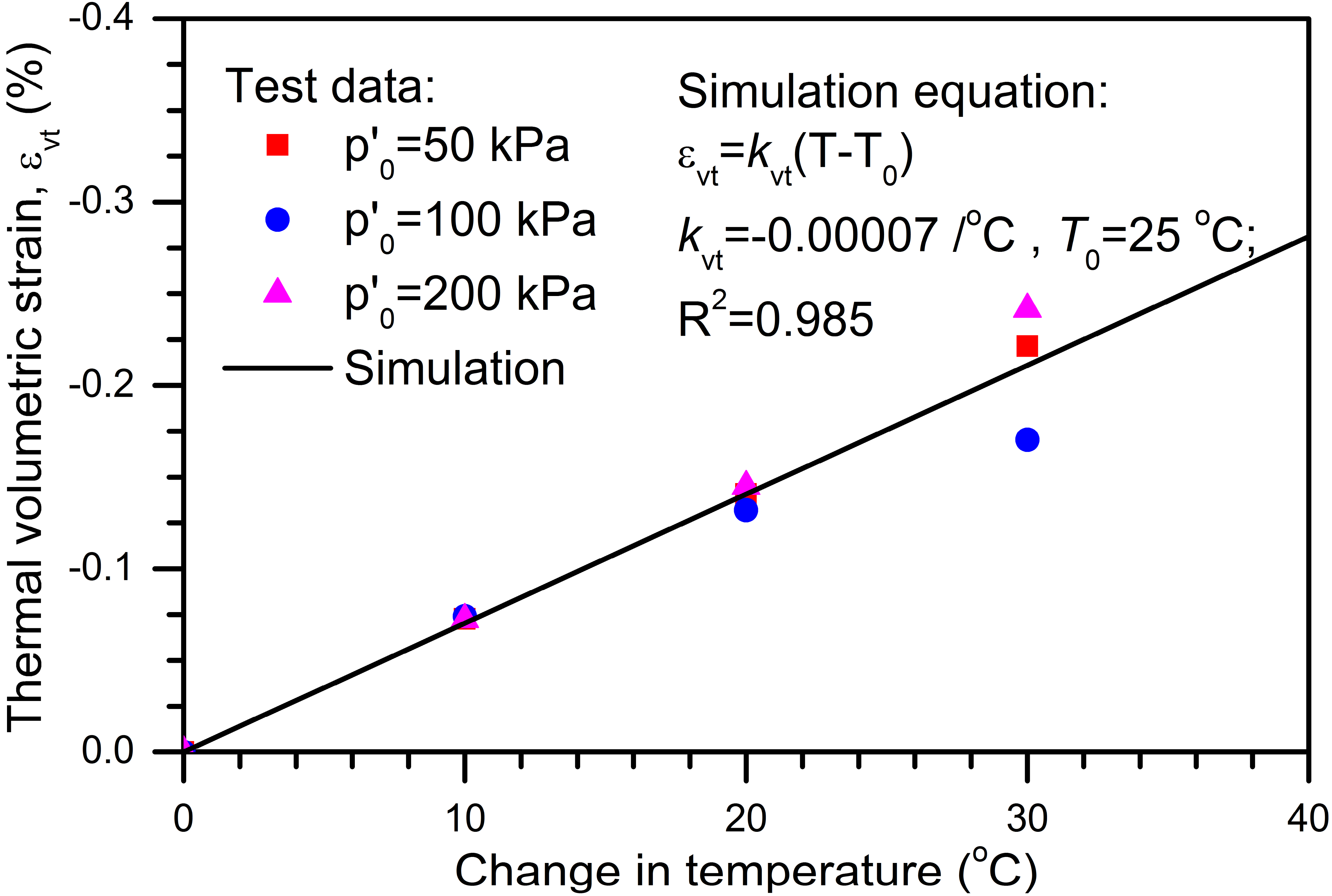
Test data:
p'0=50 kPa
p'0=100 kPa
p'0=200 kPa
Simulation
Simulation equation:
εvt=kvt(T-T0)
kvt=-0.00007 /°C , T0=25 °C;
R2=0.985
Thermal volumetric strain, εvt (%)
Change in temperature (°C)
-0.4
-0.3
-0.2
-0.1
0.0
0
10
20
30
40

Figure 3

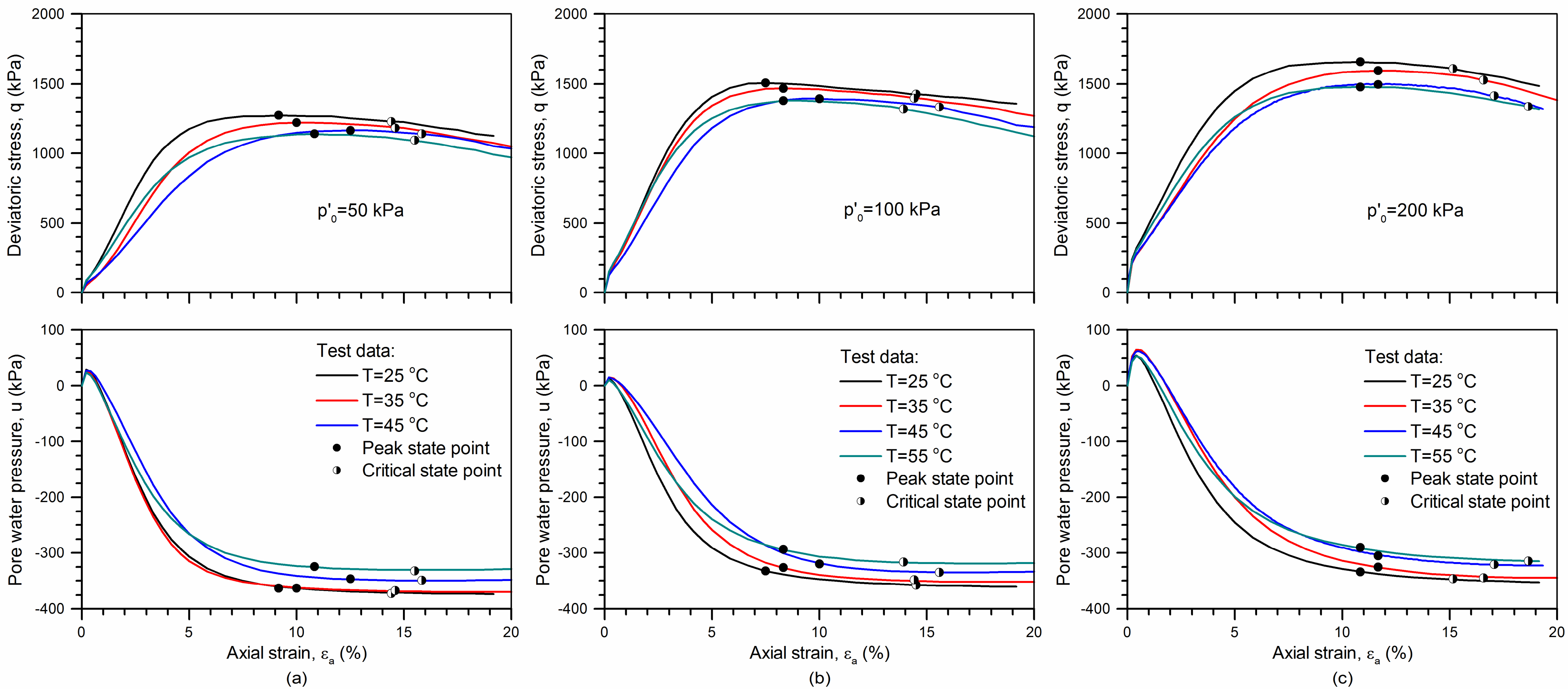

Deviatoric stress, q (kPa)
Pore water pressure, u (kPa)
Axial strain, ε_a (%)
p'$_0$=50 kPa
p'$_0$=100 kPa
p'$_0$=200 kPa
Test data:
T=25 °C
T=35 °C
T=45 °C
T=55 °C
Peak state point
Critical state point
(a)
(b)
(c)

Figure 4

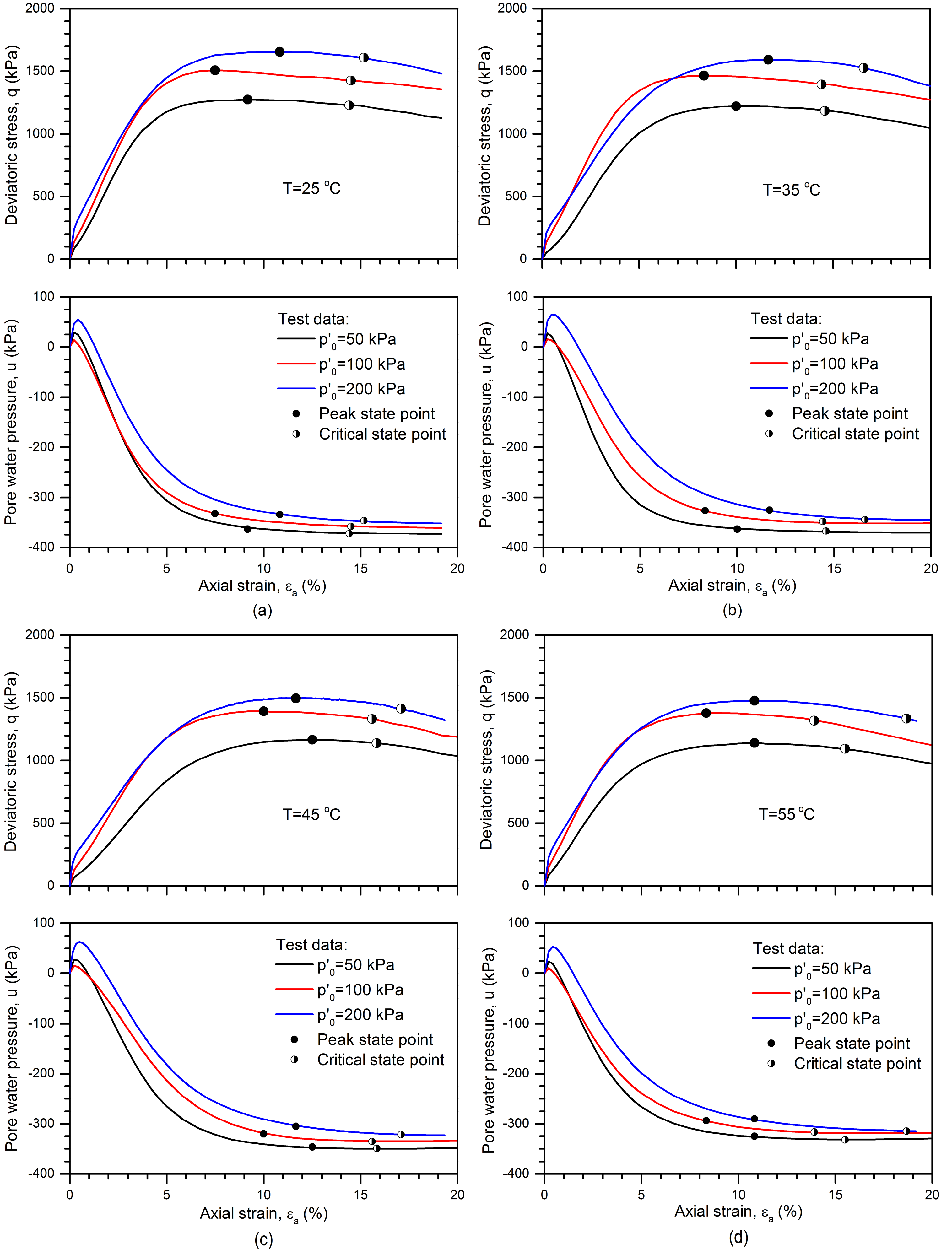

T=25 °C
T=35 °C
T=45 °C
T=55 °C
Deviatoric stress, q (kPa)
Pore water pressure, u (kPa)
Axial strain, ε_a (%)
Test data:
p'_0=50 kPa
p'_0=100 kPa
p'_0=200 kPa
Peak state point
Critical state point
(a)
(b)
(c)
(d)

Figure 5

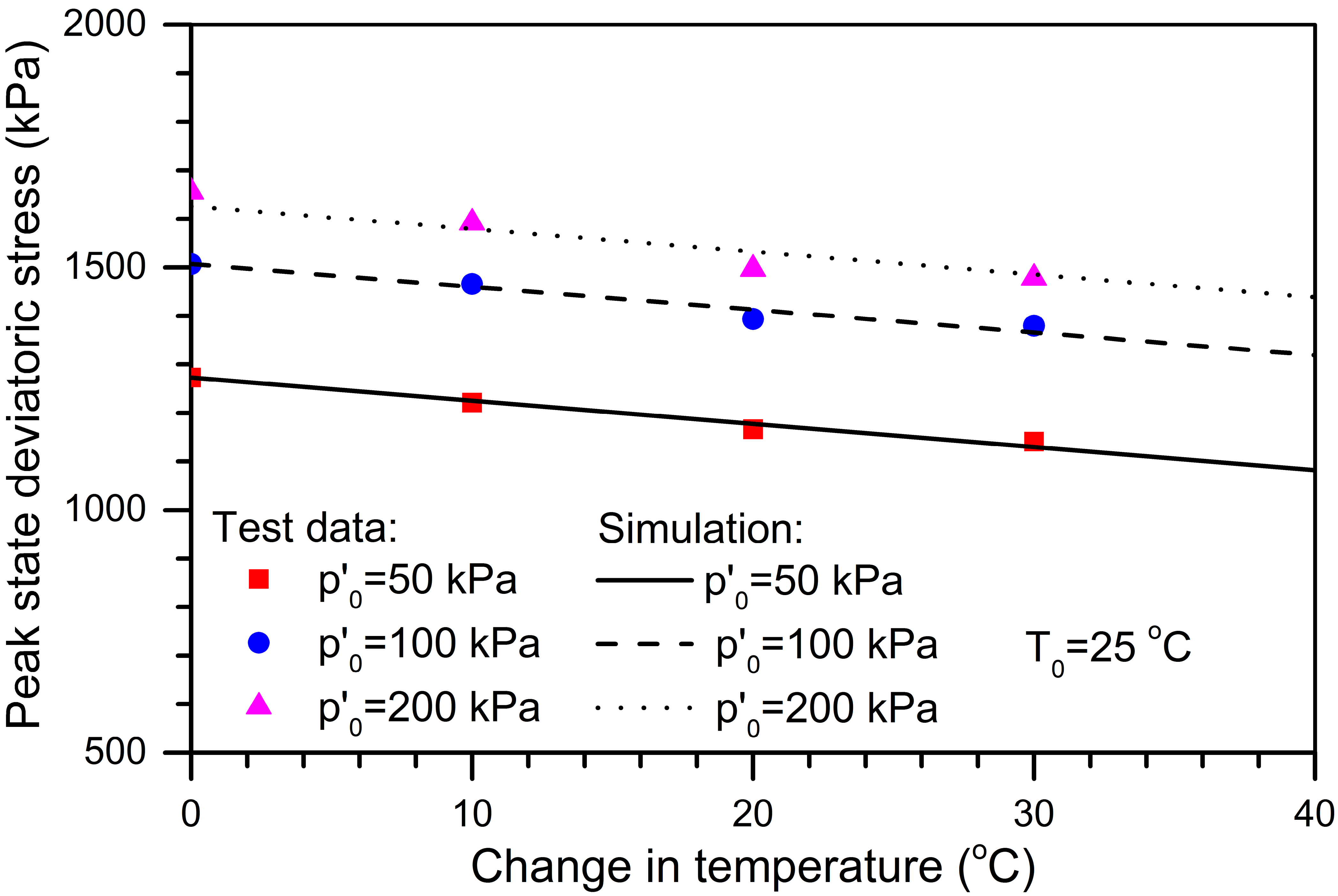

2000
1500
1000
500
0
10
20
30
40
Peak state deviatoric stress (kPa)
Change in temperature (°C)
Test data:
p'0=50 kPa
p'0=100 kPa
p'0=200 kPa
Simulation:
p'0=50 kPa
p'0=100 kPa
p'0=200 kPa
T0=25 °C

Figure 6

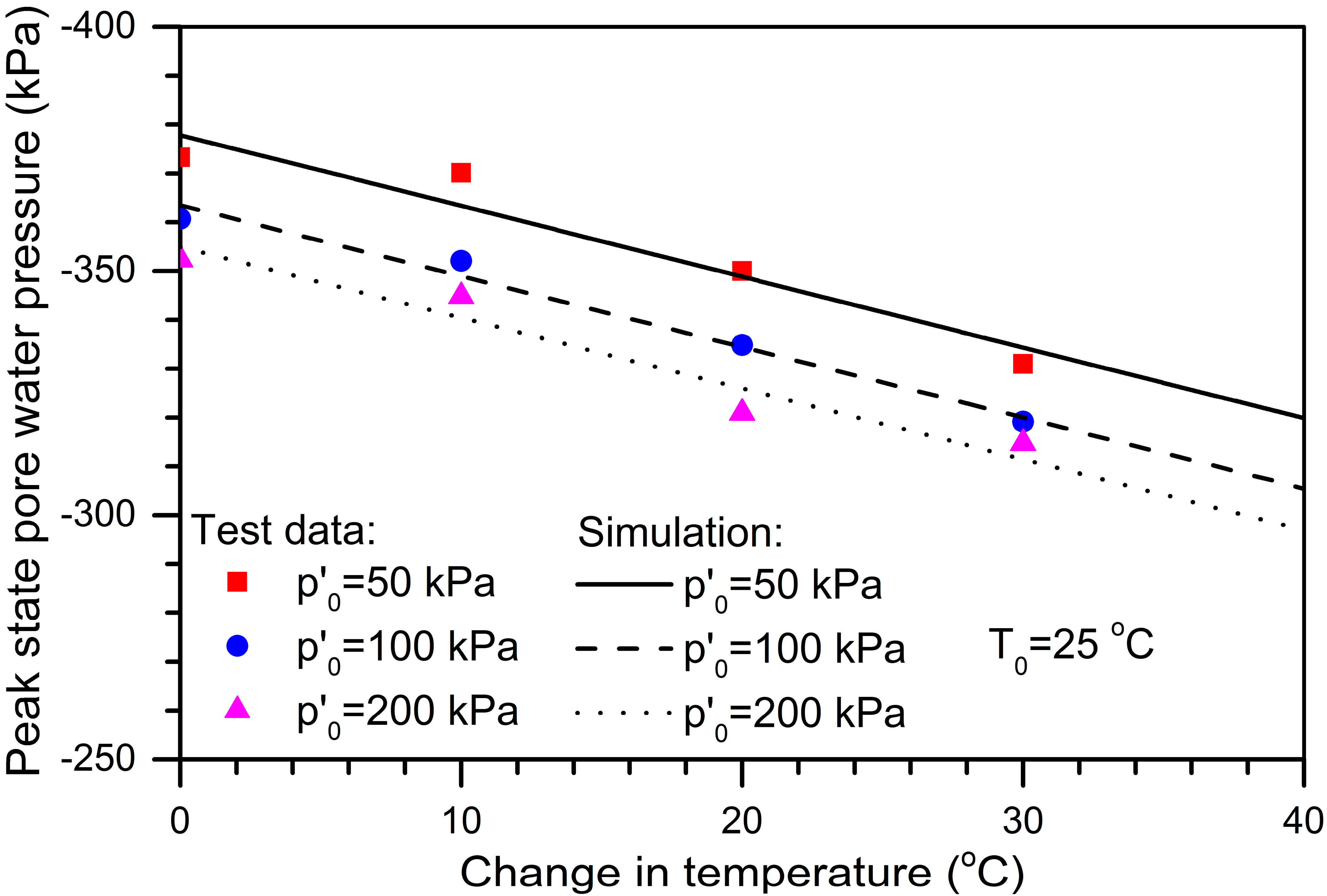

Peak state pore water pressure (kPa)
-400
-350
-300
-250
0
10
20
30
40
Change in temperature (°C)
Test data:
p'0=50 kPa
p'0=100 kPa
p'0=200 kPa
Simulation:
p'0=50 kPa
p'0=100 kPa
p'0=200 kPa
T0=25 °C

Figure 7

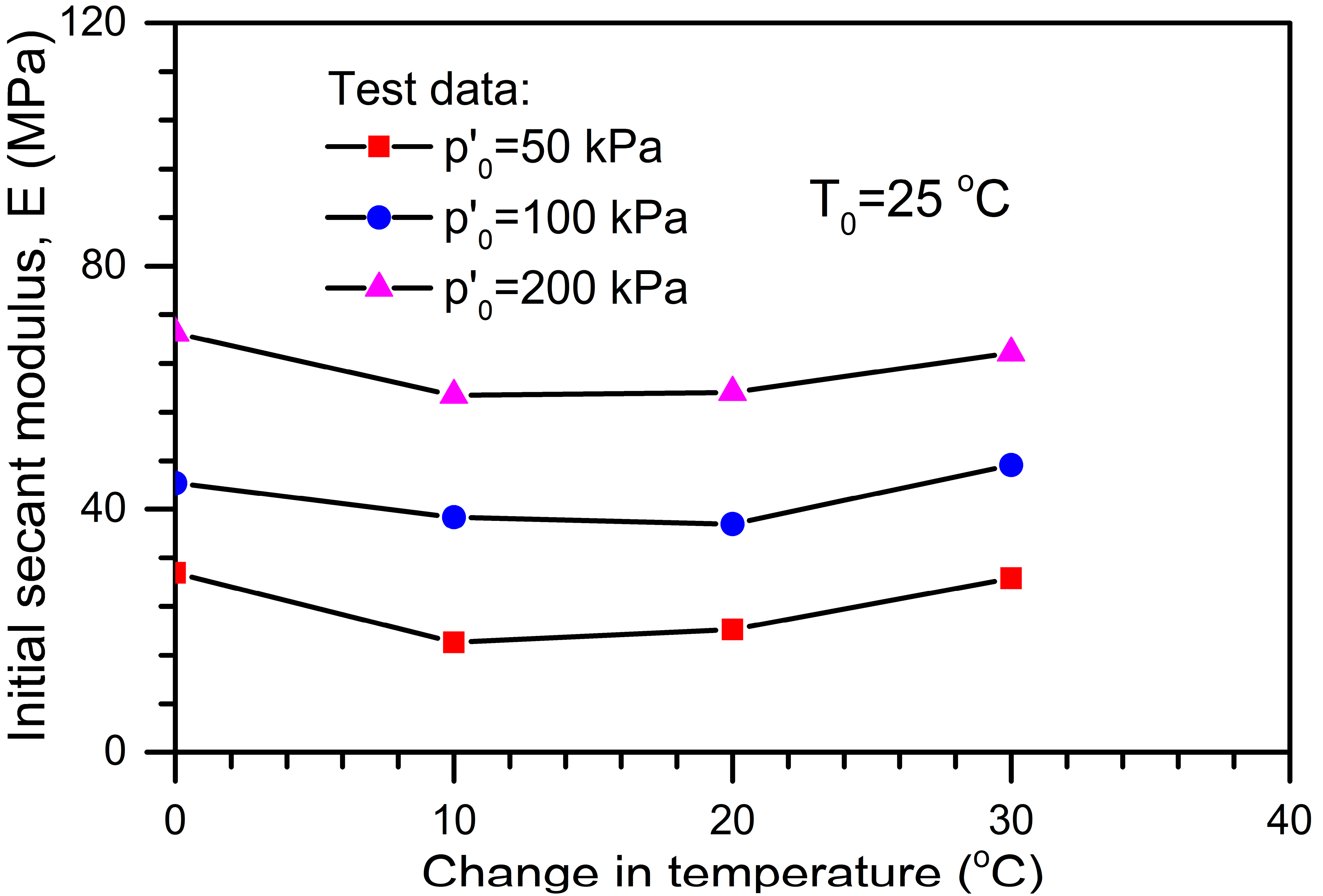

120
80
40
0
Initial secant modulus, E (MPa)
Test data:
p'0=50 kPa
p'0=100 kPa
p'0=200 kPa
T0=25 °C
0
10
20
30
40
Change in temperature (°C)

Figure 8

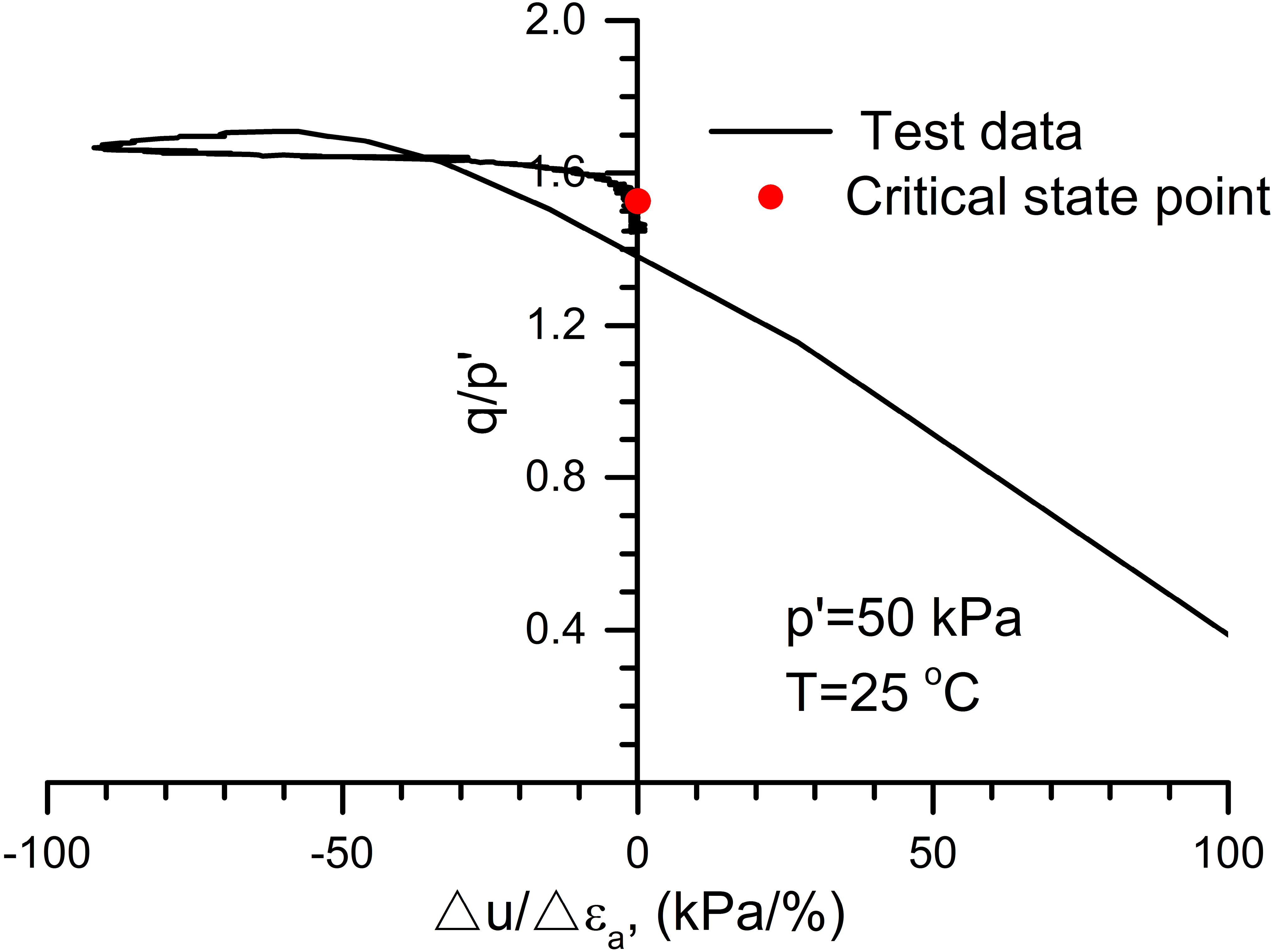

2.0
1.6
1.2
0.8
0.4
q/p'
Test data
Critical state point
p'=50 kPa
T=25 °C
-100
-50
0
50
100
△u/△ε_a, (kPa/%)

Figure 9

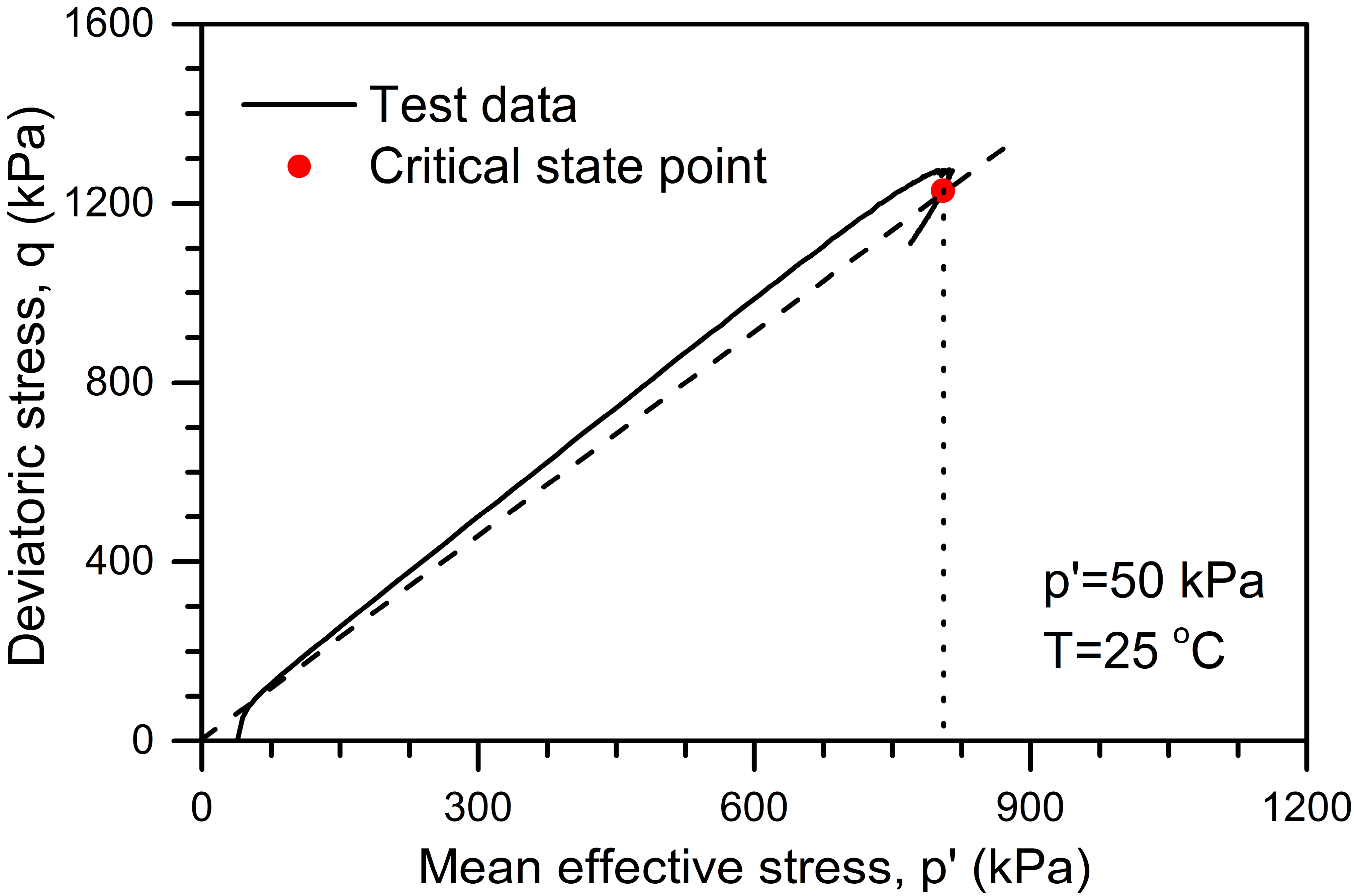

Test data
Critical state point
p'=50 kPa
T=25 °C
Deviatoric stress, q (kPa)
Mean effective stress, p' (kPa)
0
400
800
1200
1600
0
300
600
900
1200

Figure 10

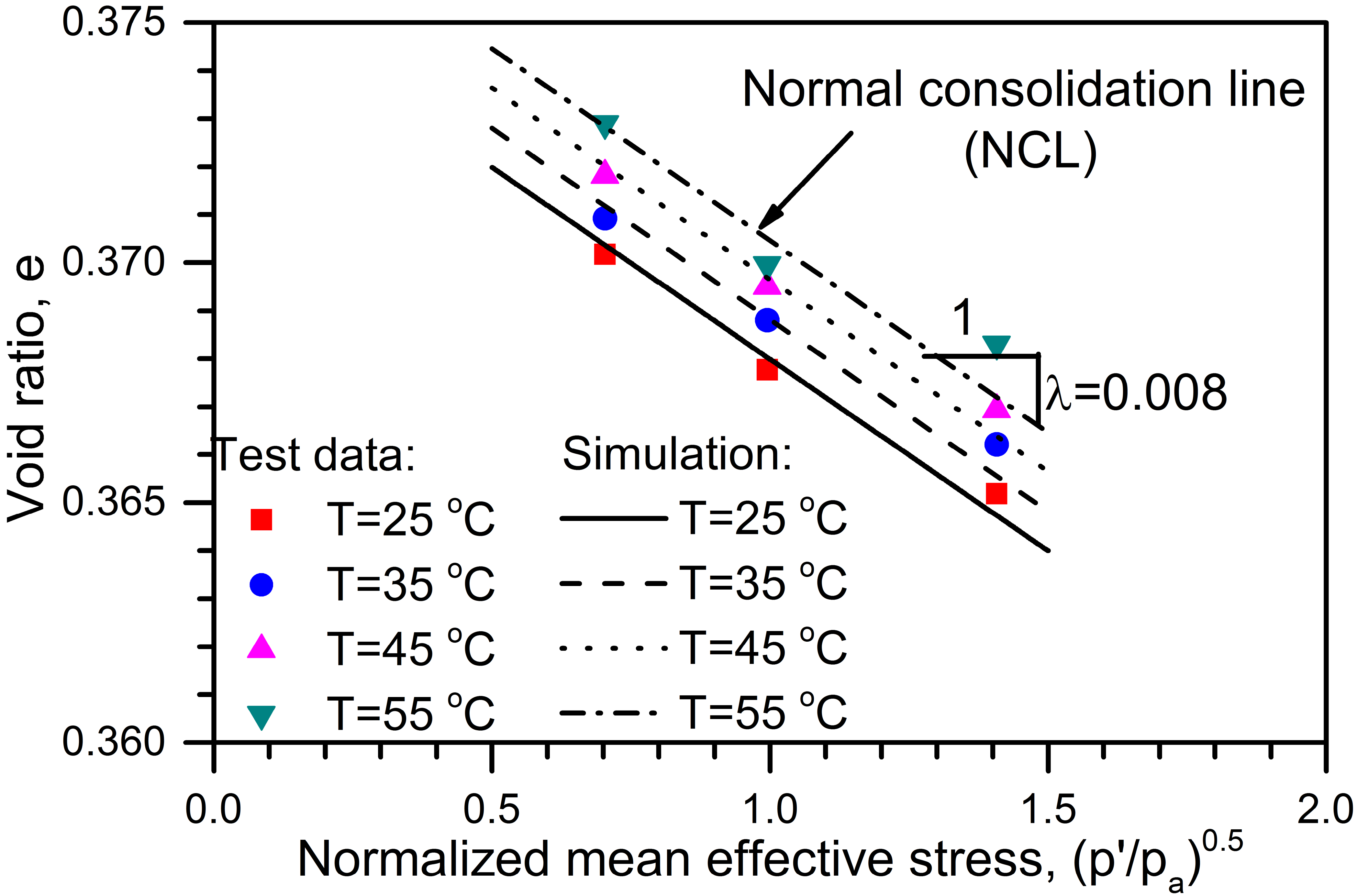

0.375
0.370
0.365
0.360
Void ratio, e
0.0
0.5
1.0
1.5
2.0
Normalized mean effective stress, (p'/p_a)^0.5
Normal consolidation line
(NCL)
1
λ=0.008
Test data:
T=25 °C
T=35 °C
T=45 °C
T=55 °C
Simulation:
T=25 °C
T=35 °C
T=45 °C
T=55 °C

Figure 11

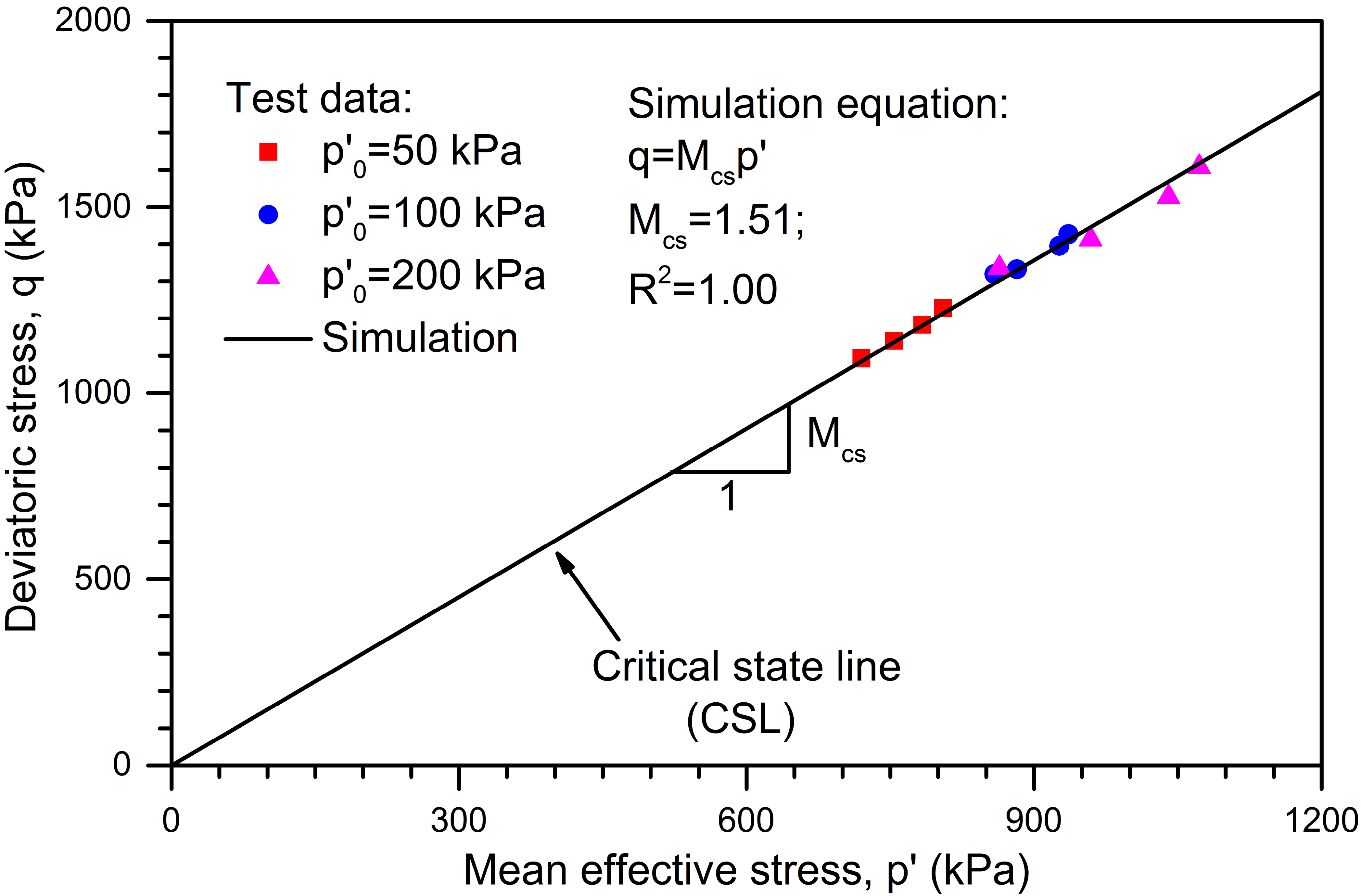

2000
1500
1000
500
0
0
300
600
900
1200
Deviatoric stress, q (kPa)
Mean effective stress, p' (kPa)
Test data:
p'0=50 kPa
p'0=100 kPa
p'0=200 kPa
Simulation
Simulation equation:
q=Mcsp'
Mcs=1.51;
R2=1.00
Mcs
1
Critical state line
(CSL)

Figure 12

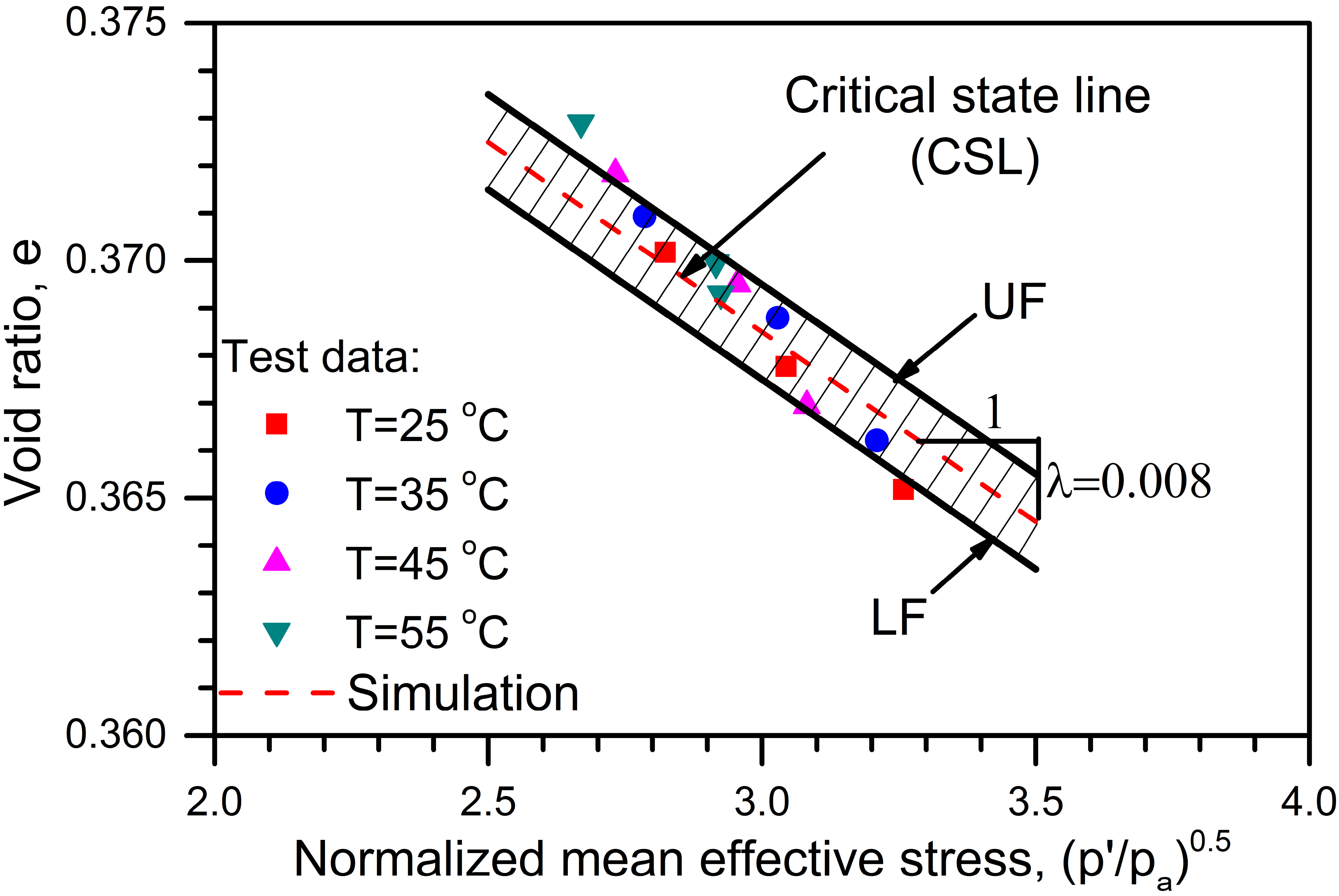

0.375
0.370
0.365
0.360
Void ratio, e
2.0
2.5
3.0
3.5
4.0
Normalized mean effective stress, (p'/p_a)^0.5
Critical state line
(CSL)
UF
LF
1
λ=0.008
Test data:
T=25 °C
T=35 °C
T=45 °C
T=55 °C
Simulation